Cobalt Metal–Organic Framework Based on Two Dinuclear Secondary Building Units for Electrocatalytic Oxygen Evolution

Silvia Gutiérrez-Tarriño,[†] José Luis Olloqui-Sariego,[‡] Juan José Calvente,[‡] Miguel Palomino,[†] Guillermo Mínguez Espallargas,[§] José L. Jordá,[†] Fernando Rey,[†] and Pascual Oña-Burgos*[,†]

[†]Instituto de Tecnología Química, Universitat Politècnica de València-Consejo Superior de Investigaciones Científicas (UPV-CSIC), Avda. de los Naranjos, s/n, 46022 Valencia, Spain

[‡]Departamento de Química Física, Universidad de Sevilla, Profesor García González, 1, 41012 Sevilla, Spain

[§]Instituto de Ciencia Molecular (ICMol), Universidad de Valencia, c/Catedrático José Beltrán, 2, 46980 Paterna, Spain

Supporting Information

ABSTRACT: The synthesis of a new microporous metal–organic framework (MOF) based on two secondary building units, with dinuclear cobalt centers, has been developed. The employment of a well-defined cobalt cluster results in an unusual topology of the **Co_2-MOF**, where one of the cobalt centers has three open coordination positions, which has no precedent in MOF materials based on cobalt. Adsorption isotherms have revealed that **Co_2-MOF** is in the range of best CO_2 adsorbents among the carbon materials, with very high CO_2/CH_4 selectivity. On the other hand, dispersion of **Co_2-MOF** in an alcoholic solution of Nafion gives rise to a composite (**Co_2-MOF**@Nafion) with great resistance to hydrolysis in aqueous media and good adherence to graphite electrodes. In fact, it exhibits high electrocatalytic activity and robustness for the oxygen evolution reaction (OER), with a turnover frequency number value superior to those reported for similar electrocatalysts. Overall, this work has provided the basis for the rational design of new cobalt OER catalysts and related materials employing well-defined metal clusters as directing agents of the MOF structure.

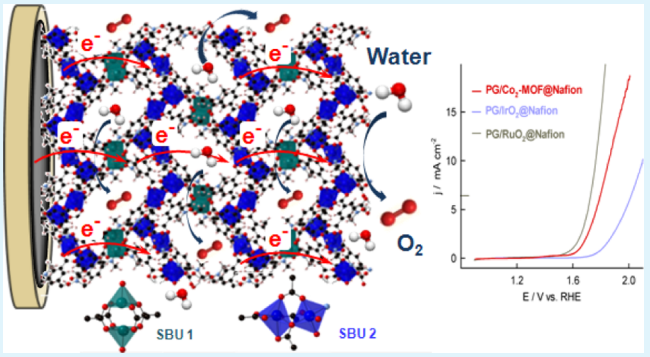

KEYWORDS: *cobalt cluster, cobalt MOF, electrocatalysis, oxygen evolution reaction and gas storage*

INTRODUCTION

Water splitting is one of the key processes for many applications related with energy storage and conversion.[1−3] Water oxidation (WO) or oxygen evolution reaction (OER) is still considered the most challenging step in water splitting as it is a more complex transformation than proton reduction.[4,5] In fact, OER is essential to achieve successful hydrogen production from water[6,7] but also in other applications such as regenerating fuel cells[8] and rechargeable metal–air batteries.[9] Cobalt-based WO catalysts (WOC), including molecular complexes[5,10,11] and inorganic nanoparticles,[12−17] are of great interest because of their prominent activities and abundance of this metal in the earth.[18−21]

However, few examples of electrocatalytic WOC based on porous metal–organic frameworks (MOFs)[22] have been reported,[23−26] despite their large structural features. In fact, the ample versatility in coordination modes and nuclearity has provided a high structural diversity of MOFs in barely 25 years, with applications in the fields of gas storage and sensing,[27−29] catalysis,[30,31] and electroactive materials in devices.[31−36] In addition, MOFs are also emerging as potential electrocatalysts for CO_2 reduction, hydrogen evolution reaction and OER.[37−39]

Among the different secondary building units (SBUs) that form MOFs, the dinuclear $M_2(RCOO)_4$ paddlewheel (M = Cu, Zn, Ni, Fe, Co, Mo, Cr, Ru) is considered a potential core to achieve OER successfully with abundant metallic elements.[40] However, cobalt MOF materials based on this SBU have shown poor stability in water.[41] Different approaches have been used to augment the water stability of MOFs mainly based on the employment of bulky, hydrophobic, and/or irremovable ligands.[40,42,43] Herein, we report a new Co-based MOF of formula $\{[Co_2(BTC)_{1,3}(DMF)_2]$-$[Co_2(BTC)_{1,3}(DMF)_2py]\}$, denoted as **$Co_2$-MOF**, possessing two distinct dinuclear cobalt SBUs. Upon Nafion coating, **Co_2-MOF** is water-stable, thus allowing its evaluation as an electrocatalyst in the OER with high activity under mild conditions.

DISCUSSION AND RESULTS

Synthesis and Characterization of Co_2-MOF. The solvothermal reaction of the cubane cluster $[Co_4O_4(OAc)_4(Py)_4]$[44] and benzene tricarboxylic acid (H_3BTC) in DMF results in the formation of violet plates of **Co_2-MOF** after 72 h. The use of the cubane cluster as a starting material is key for the formation of **Co_2-MOF**, unachievable with other common cobalt reagents. Single-crystal X-ray diffraction (Figures S1 and S2) reveals that **Co_2-MOF** crystallizes in the monoclinic $P2_1/n$ space group (Table S1). Two different dinuclear SBU, denoted SBU1 and SBU2, are found in this structure (Figure 1). The SBU1 unit is the

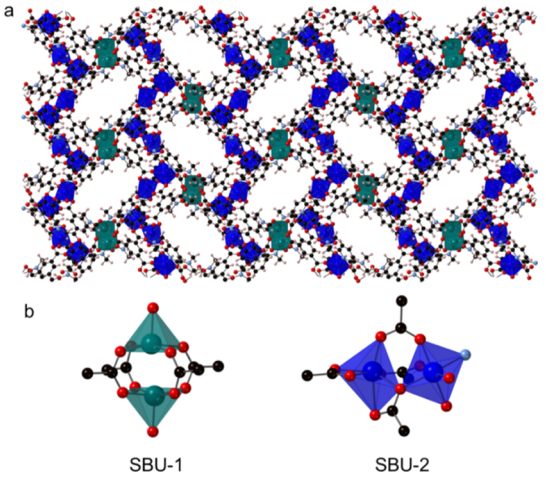

Figure 1. (a) Crystal structure of **Co_2-MOF**; (b) representation of the two dimeric SBUs found in compound 1: SBU1, the characteristic paddlewheel unit, and SBU2, with an unusual coordination of three solvent molecules to one metal center. Hydrogen atoms are omitted for clarity.

archetypal paddlewheel structure, formed by two crystallographically related Co^{2+} atoms (via an inversion center, more details in the Supporting Information). The SBU2 unit is more atypical, formed by two crystallographically independent Co^{2+} atoms, each of them with a different connectivity. One Co center is coordinated by six oxygen atoms from four BTC^{3-} ligands, with Co−O distances in the range of other reported cobalt MOFs (Figure S3).[45−50] Specifically, there are two ligands that chelate the metal center, whereas the other two ligands coordinate in the classical way of a paddlewheel structure. The other Co center of the SBU2 unit is coordinated by three O atoms from three shared BTC^{3-} ligands and three solvent molecules (one pyridine molecule and two DMF molecules), with distances in the range of other reported cobalt MOFs (Figure S3b).

The connection of these two different SBUs yields a 3D network with 1D channels parallel to the crystallographic a axis (Figure S4), which are filled with DMF molecules, as confirmed by thermogravimetric analysis (TGA, Figure S5). The microporosity of the material has been demonstrated upon activation at 100 °C under vacuum, with a high CO_2 adsorption capacity of 1.1 mmol/g at 0 °C and 100 kPa (Figure S6a,b), which corresponds to an apparent surface area of 233 m^2/g. The value of the isosteric heat of adsorption of CO_2 at zero coverage ($q_{st,0}$) calculated from the Henry constants is 30 kJ/mol (Figure S6c), being comparable to the one of an LTA (Linde Type A) zeolite with a Si/Al ratio of 5.[51] This value was set as a good compromise between adsorption capacity and regenerability for a CO_2 adsorbent because of the strength of the gas−solid interactions. The high-pressure CO_2 and CH_4 isotherms (up to 10 bar) obtained at different temperatures (Figures S6d) support **Co_2-MOF** as a promising material for CO_2/CH_4 separation (Figure S6e) with very similar values to those of zeolitic molecular sieves.[52] Although the selectivity decreases with the increase of pressure, it remains very high, even at 298 K and 500 kPa. Magnetic measurements of **Co_2-MOF** (Figure S7) were also employed to characterize this new material. Finally, **Co_2-MOF** was studied by field emission scanning electron microscopy (FESEM) and energy-dispersive X-ray spectroscopy (EDX) analysis (Figure S8) to provide further composition characterization, and by X-ray photoelectron spectroscopy (XPS) to know more about the electronic structure. The photoelectron spectra of the Co 2p line for the **Co_2-MOF** (Figure S9) and the fitting results are shown in Table S2. From this analysis, it could be confirmed that cobalt centers are exclusively in the Co(II) oxidation state.

Chemical Stability of Co_2-MOF. Despite the high thermal stability of **Co_2-MOF**, a structural reorganization takes place in the presence of protic solvents such as ethanol, water, and their mixtures (Figures S10 and S11). Thus, **Co_2-MOF** is transformed into a previously described mononuclear cobalt material of formula $Co_3(BTC)_2(H_2O)_3$, denoted as **Co-MOF**.[53] This material forms a hydrogen-bonded 3D structure based of zig-zag chains in which coordinated water molecules interact with carboxylate groups of adjacent chains. In an effort to overcome this drawback, we have found that its dispersion in an alcoholic Nafion solution provides a composite (**Co_2-MOF**@Nafion) that is stable in water, as evidenced by the absence of significant changes in the X-ray power diffraction patterns measured for **Co_2-MOF**@Nafion before and after being treated with water (Figures S12 and S13). According to recent studies with HKUST-1/Nafion and Zn(II) based MOF/Nafion composites,[54,55] the enhancement of the MOF chemical stability can be ascribed to a lower water content in the composite compared to that in the absence of Nafion. These studies reported on a decrease of the water uptake by the composite upon increasing the amount of MOF, which was ascribed to the reduction of the number and size of the available pores. Apart from its protective role, Nafion also improves the adherence of **Co_2-MOF** to graphite electrodes, enabling the study of its electrocatalytic performance for the water oxidation (vide infra).

Electrochemical Study of Co_2-MOF and Co-MOF. The electrochemical behavior of **Co_2-MOF** was investigated by cyclic voltammetry (CV) employing a pyrolytic graphite electrode coated with a **Co_2-MOF**@Nafion film in a solution containing 0.1 M $[Et_4N]BF_4$ in acetonitrile (Figure 2a). The voltammogram consists of two well-resolved quasireversible waves at 1.02 V (wave I) and 1.35 V (wave II), superimposed to a rising background current. To get some clues of the redox conversion involved in each voltammetric wave, the voltammetric response of the mononuclear **Co-MOF** has been measured (Figure 2a). It also shows two well-resolved voltammetric waves located at 0.61 and 1.35 V, which correspond to the two consecutive monoelectronic redox conversions Co(II)/Co(III) (wave I) and Co(III)/Co(IV) (wave II), respectively (scheme in Figure 2b). The similarity of the charge under the baseline-corrected voltammetric waves for both MOFs suggests that monoelectronic charge transfers

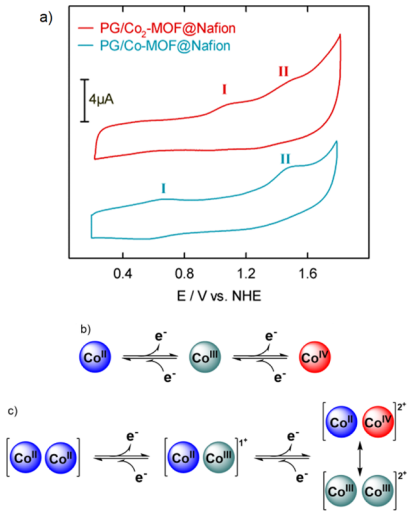

Figure 2. (a) Cyclic voltammograms of a pyrolytic graphite electrode modified with **Co_2-MOF**@Nafion (red line) or hydrolyzed **Co-MOF**@Nafion (cyan line) recorded at 0.05 V s^{-1} in a solution containing 0.1 M $[Et_4N]BF_4$ in acetonitrile at 25 °C. (b,c) Redox conversions involved in the voltammetric response of coated (b) **Co-MOF** and (c) **Co_2-MOF**.

are also taking place in the **Co_2-MOF**, the first being ascribed to the Co(II)/Co(III) redox conversion. For the second wave, however, there are two plausible scenarios, namely, (i) the Co(II)/Co(III) redox conversion of the second cobalt center or (ii) the Co(III)/Co(IV) redox conversion of the Co(III) center formed in the first anodic wave (scheme in Figure 2c). Although we cannot discriminate among these two possibilities, the similarity of the peak potential values for the second anodic wave of both **Co-MOF** and **Co_2-MOF** suggests that it may also correspond to the Co(III)/Co(IV) redox conversion for the dinuclear **Co_2-MOF**. Nevertheless, it cannot be overlooked that both species Co(II)−Co(IV) and Co(III)−Co(III) could coexist in equilibrium as Nocera et al. have proposed recently for other dinuclear cobalt OER catalysts based on their specific electronic features.[56,57]

Additionally, it has been found that increasing the scan rate from 0.002 to 0.2 V s^{-1} results in a decrease of the faradaic voltammetric charge from ∼7.5 to ∼0.6 μC (Figures S14 and S15). This finding is consistent with a progressive limitation of the redox conversion by charge transport across a multilayered film.[58,59] In addition, the small variation of the anodic peak potentials with the scan rate (Figures S14 and S15) is indicative of different local environments for the cobalt center along the film. Moreover, it should be noted that upon extending the potential scan to more negative values, two additional cathodic voltammetric waves at −0.450 and −0.870 V (vs NHE, Normal Hydrogen Electrode), with their corresponding anodic waves at −0.317 and −0.080 V (vs NHE), appear (Figure S16). The fact that the more negative cathodic wave also appears in the **Co_2-MOF**-free Nafion-coated graphite electrode reveals that only the first cathodic wave at −0.450 V can be ascribed to the reduction of the cobalt centers. The similarity of its baseline-corrected charge with the total charge exchanged in the two anodic waves preceding the OER signal suggests that it corresponds to the two monoelectronic Co(II)−Co(II)/Co(I)−Co(I) redox conversions.

On the other hand, as shown in Figure 2a, the second redox conversion of the two cobalt MOFs is accompanied by a significant increase of the background current. The fact that this component of the overall current increases upon addition of variable volumes of an aqueous sodium phosphate buffer (SPB) solution of pH 7 (Figure 3a) indicates that it

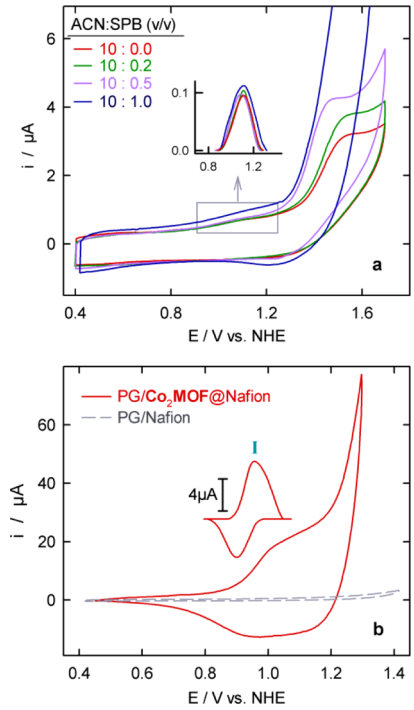

Figure 3. (a) Cyclic voltammograms of the **Co_2-MOF**@Nafion-modified pyrolitic graphite electrode recorded at 10 mV s^{-1} for the indicated acetonitrile/aqueous SPB solution (pH 7) ratio. (b) Cyclic voltammograms of a pyrolytic graphite electrode modified with Nafion (dashed gray line) or **Co_2-MOF**@Nafion (red line) recorded at 10 mV s^{-1} in an aqueous solution containing 0.1 M SPB, pH 7, at 25 °C.

corresponds to the **Co_2-MOF**-mediated electrocatalytic oxidation of water, commonly known as the OER. The insensitivity of the voltammetric wave I to the presence of increasing amounts of water reveals that Nafion not only serves to anchor **Co_2-MOF** to the electrode surface, but also to preclude its hydrolysis, as otherwise a shift of this voltammetric wave toward the one observed for the hydrolyzed **Co-MOF** would be expected.

Figure 3b illustrates the voltammetric response of **Co_2-MOF** deposited onto a graphite electrode measured in a deaerated 0.1 M SPB solution of pH 7. Only one voltammetric wave (wave I) is observed at 0.98 V (vs NHE) because of the broad overlapping of the exponentially increasing OER electrocatalytic current with the voltammetric wave associated with the second redox conversion. Under these conditions, the scan rate dependence of the voltammetric peak parameters of wave I is similar to that found in acetonitrile (Figure S17), so that the rate of the redox conversion is limited by charge transport across the film, and different local environments exist for the cobalt centers along the film.[58,59]

Electrocatalytic Performance for the OER. To explore the electrocatalytic activity of **Co_2-MOF** toward the OER in neutral media, rotating disk voltammetry was employed to obtain nearly steady-state polarization curves. All measure-

ments were carried out with a scan rate of 5 mV s^{-1} and a rotation rate of 4000 rpm, to preserve a uniform concentration profile around the working electrode and to prevent the accumulation of O_2 bubbles. A typical polarization curve is depicted in Figure 4a, which shows a sharp rise of the anodic

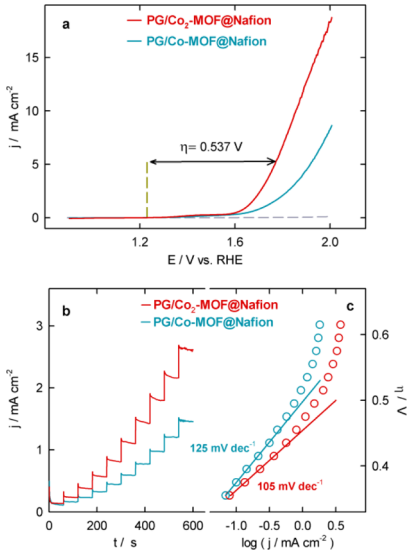

Figure 4. (a) Rotating disk voltammograms of a pyrolytic graphite electrode modified with **Co_2-MOF**@Nafion (red line) or hydrolyzed **Co-MOF**@Nafion (cyan line) recorded at 5 mV s^{-1} and 4000 rpm in an aqueous solution containing 0.1 M SPB, pH 7, at 25 °C. The dashed gray line is the corresponding cyclic voltammogram of a pyrolytic graphite electrode modified with Nafion. (b) Potentiostatic chronoamperograms of a pyrolytic graphite electrode modified with **Co_2-MOF**@Nafion (red line) or **Co-MOF**@Nafion (cyan line) recorded at 4000 rpm for incremental potential steps of 0.02 V, from 1.59 to 1.85 V, in an aqueous solution containing 0.1 M SPB, pH 7, at 25 °C. (c) Tafel plots of the steady-state current density data of (b).

current at 1.68 V (vs RHE, Reversible Hydrogen Electrode) that is associated with the onset of the electrocatalytic OER, whereas there is no appreciable current signal in the absence of the catalyst. In the same experimental conditions, the hydrolyzed mononuclear **Co-MOF** produces smaller electrocatalytic currents, with almost the same onset potential as its dinuclear counterpart **Co_2-MOF**. The similarity between their electrocatalytic onset potentials and their redox potential for the Co(III)/Co(IV) conversion suggests that the electrocatalytic oxidation of water is driven by Co(IV). An important operating parameter for the OER performance evaluation is the overpotential at a fixed current. Taking the thermodynamic OER potential value of 1.23 V (vs RHE) as reference, the PG/**Co_2-MOF**@Nafion electrode shows overpotential values of 460 and 537 mV at 2 and 5 mA cm^{-2}, respectively. These overpotential values are lower than those determined for the mononuclear **Co-MOF** (565 and 687 mV at 2 and 5 mA cm^{-2}, respectively) and those previously reported for MOF-based catalysts operating in neutral media, with the exception of the hybrid MOF MCF-49[60] (Table S3 in the Supporting Information). Moreover, a comparison of the polarization curve of **Co_2-MOF** with those obtained for the well-known IrO_2 and RuO_2 OER electrocatalysts reveals the excellent OER performance of the herein constructed cobalt-based MOF (Figure S18 in the Supporting Information).

The electrocatalytic kinetics of the OER was estimated from the corresponding Tafel plot obtained from the steady-state current density data recorded in the 1.59−1.85 V (vs RHE) potential range by means of potentiostatic chronoamperometry, with a potential step of 0.02 V (Figure 4b). At least three **Co_2-MOF**@Nafion electrode replicates were used in the chronoamperometric measurements for the determination of the Tafel slope, with an electroactive cobalt surface concentration (Γ) in the $15 < \Gamma < 30$ nmol cm^{-2} range. **Co_2-MOF** exhibits a Tafel slope of 105 ± 5 mV $decade^{-1}$ in 0.1 M SPB pH 7, being to our knowledge the best value among known cobalt MOF catalysts[60] (Table S3 in the Supporting Information). In the same experimental conditions, the Tafel slope for the mononuclear **Co-MOF** is 125 ± 5 mV $decade^{-1}$.

The turnover frequency (TOF) number was determined from the expression $TOF = jA/(4Fm)$, where j is the current density at a given overpotential, A is the geometrical surface area of the graphite electrode, F is the Faraday constant, and m is the mole number of electroactive cobalt participating in the catalytic process. The amount of electroactive cobalt was determined from $m = Q/(nF)$, where Q is the faradaic charge under the baseline-corrected voltammetric peak preceding the electrocatalytic wave, and n is the number of electrons transferred per cobalt center. A value of 0.026 ± 0.005 s^{-1} was obtained for the TOF number of **Co_2-MOF** at an overpotential of 400 mV with $m = 1.70 \times 10^{-9}$ mol and $n = 1$ (Figure 4c). This value is superior to the one determined for the mononuclear **Co-MOF** (0.014 ± 0.005 s^{-1} with $m = 1.75 \times 10^{-9}$ mol and $n = 1$) and to those values reported for similar electrocatalysts (Table S3 in the Supporting Information).

The influence of the redox electroactive surface concentration of **Co_2-MOF** on the electrocatalytic water oxidation was also evaluated. Figure 5a shows how the current density

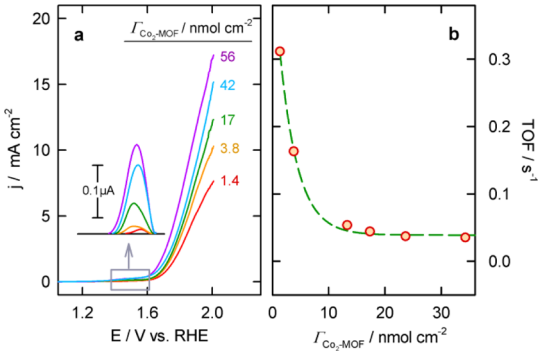

Figure 5. (a) Rotating-disk voltammograms of a pyrolytic graphite electrode modified with different electroactive amounts of **Co_2-MOF**@Nafion in the $0.1-3.9 \times 10^{-9}$ mol number range, recorded at 5 mV s^{-1} and 4000 rpm in an aqueous solution containing 0.1 M SPB, pH 7, at 25 °C. Inset plot: Baseline-corrected voltammetric wave I. (b) Estimated TOF number at an overpotential of 400 mV as a function of electroactive cobalt surface concentration. The green dashed line is just an eye guide.

increases and the corresponding overpotential at a given current density decreases upon raising the redox electroactive surface concentration. As shown in Figure 5b, the estimate TOF number for **Co_2-MOF** at an overpotential of 400 mV decreases upon increasing the catalyst loading, until it levels off at ~0.045 s^{-1} for a surface concentration of redox active cobalt of 1.7×10^{-8} mol cm^{-2}. This leveling-off effect may result from agglomeration of the catalyst grains upon increasing their

surface concentration, which may limit the solvent-exposed catalytic surface area and change the surface mass transport regime from cylindrical to planar symmetry.

To assess the stability of the electrocatalyst during the OER, we have compared the polarization curves measured before and after performing 500 consecutive cyclic voltammograms in the 0.8−1.9 V (vs RHE) potential window, at a sweep rate of 0.2 V s^{-1}. As shown in Figure 6a, the polarization curve barely

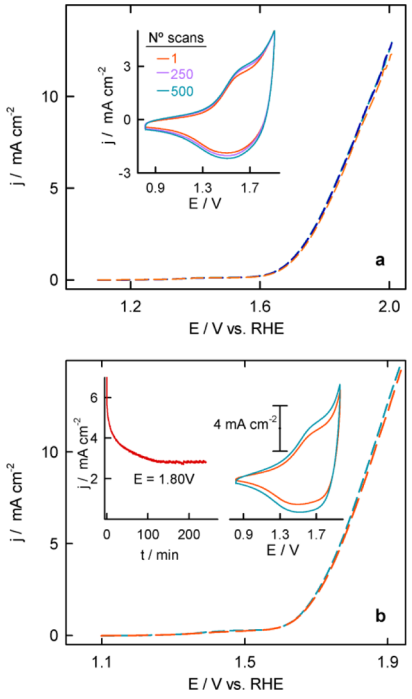

Figure 6. (a) Rotating disk voltammograms for a **Co_2-MOF**@Nafion-modified graphite electrode measured at 5 mV s^{-1} after recording 1 scan (dashed orange line), 20 consecutive scans (dashed blue line), and 500 consecutive scans (dashed cyan line) at 0.2 V s^{-1} in an aqueous solution containing 0.1 M SPB, pH 7, at 25 °C. Inset plot: Voltammograms recorded at the indicated number of scans with 0.2 V s^{-1}. (b) Rotating disk voltammograms for a **Co_2-MOF**@Nafion-modified graphite electrode measured at 5 mV s^{-1} before (dashed orange line) and after (dashed cyan line) recording the chronoamperometric current at 1.80 V vs RHE for 4 h is depicted in the inset plot. The corresponding cyclic voltammograms at 0.2 V s^{-1} before (orange line) and after (cyan line) the electrolysis experiment are depicted in the inset plot.

changes after this extensive cycling. Moreover, the robustness and long-term durability of the catalyst have been evaluated under operating conditions by recording the chronoamperometric current at 1.80 V for 4 h (inset of Figure 6b). As shown in the inset of Figure 6b, the chronoamperogram is characterized by an initial decrease of the current until it approaches a steady-state value of ∼55% of the initial current at long times. The invariance of the voltammograms recorded before and after the chronoamperometric experiment (Figure 6b) reveals that the decrease of the chronoamperometric current is not due to a loss of **Co_2-MOF**, but to mass transport limitation within the multilayered film. Formation of oxygen microbubbles at the electrode surface may affect water transport inside the film. Nevertheless, the preservation of the voltammetric features after such a long-term electrolytic experiment proves the good stability of the catalyst. In order to estimate the Faraday efficiency of **Co_2-MOF** for OER, the oxygen production during the water electrolysis Δm_{O_2} has been measured with a polarographic oxygen sensor. A Faraday efficiency of 87% was determined from the slope of the plot of Δm_{O_2} against the charge consumed during the electrolysis Q as illustrated in Figure S19, indicating that the current intensity mostly originates from water oxidation as evidenced by the formation of oxygen bubbles on the electrode surface (Figure S20 in the Supporting Information).

Finally, it should be noted that the present **Co_2-MOF** retains its electrocatalytic activity and stability toward the OER in aerated conditions (Figure S21), which is demanded for practical applications. Moreover, the stability of **Co_2-MOF**@Nafion after water electrolysis has been proved by employing XPS and EDX analyses (Figures S22 and S23, respectively). EDX (Figure S23) shows that cobalt is well distributed on the composite as happened in **Co_2-MOF**, and metal aggregations are not detected. In addition, XPS data of the composite (Figure S22, Table S4) support that cobalt remains in the same oxidation state and the small shift appreciated (1.4 eV) in E_b Co 2p is associated with the presence of fluorine in the composite. It is well known that fluorine tends to induce large chemical shifts in other elements.

CONCLUSIONS

In summary, we have developed the synthesis of a new microporous MOF based on two SBU with dinuclear cobalt centers. In this sense, the employment of a well-defined cobalt cluster drives force an unusual topology for **Co-MOFs**, where one of the cobalt has three open coordination positions, which has no precedent in MOF materials based on cobalt. In addition, the largest channel size is in the range of 10−12 Å. Adsorption isotherms have revealed that **Co_2-MOF** is selective for CO_2 adsorption versus CH_4 with similar values to those of zeolitic molecular sieves. Dispersion of **Co_2-MOF** in an alcoholic solution of Nafion gives rise to a composite (**Co_2-MOF**@Nafion) with a high resistance to hydrolysis in aqueous media. The obtained composite shows good adherence to graphite electrodes, where it exhibits a high electrocatalytic performance for water oxidation in neutral media, with a TOF value superior to the one determined for the mononuclear **Co-MOF** and to those reported for similar electrocatalysts. Overall, this work has provided a basis for the rational design of new cobalt OER catalysts and related materials employing well-defined metal clusters as directing agents of the MOF structure.

EXPERIMENTAL SECTION

All chemicals were purchased from the Sigma-Aldrich Chemical Co. and used as received. $[(Co_4O_4)(OAc)_4(Py)_4]$ was synthesized according to published procedures.[44]

Synthesis of Co_2-MOF. Solvothermal conditions were employed to generate **Co_2-MOF** using $[(Co_4O_4)(OAc)_4(Py)_4]$[44] as a building block of the final materials. It was synthesized from 2.7 equiv of H_3BTC (2.38 mmol) per each equivalent of $[Co_4O_4(OAc)_4(Py)_4]$ (0.89 mmol), which were dissolved in two different solutions with 25 mL of DMF each. The two solutions were mixed and 8 equiv of trifluoroacetic acid were added to reaction mixture. The resulting solution was introduced into a stainless-steel autoclave, being heated at 135 °C for 72 h under autogeneous pressure and static conditions. Once cooled to room temperature, the solution was filtered and the collected purple crystals were washed with acetone in order to remove the remaining DMF solvent molecules. Finally, the material was isolated and dried under vacuum at room temperature. Anal. Calcd for

$C_{35}H_{39}Co_3N_5O_{16}$: C, 43.676; H, 4.084; N, 7.276; Co, 18.369. Found: C, 43.947; H, 4.005; N, 7.593; Co, 18.570.

Chemical Analysis. Elemental analysis of nitrogen, carbon and hydrogen (N, C, H) contents of isolated solid materials were determined with a Carlo Erba 1106 elemental analyzer using sulfanilamide as a reference. Also, a Varian 715-ES inductively coupled plasma atomic emission spectrometer was used in order to determine the content of Co. (More information in the Supporting Information.)

Thermogravimetric Analysis. It was carried out in a Netzsch TGA/STA 449 F2 Jupiter apparatus, using a heating rate of 10 °C/min in an air stream of 100 mL/min until a temperature of 600 °C was reached.

X-ray Powder Diffraction. The X-ray diffraction measurements were acquired according to the powder method, in Bragg−Brentano geometry using a CUBIX diffractometer from PANalytical equipped with a PANalytical X'Celerator detector. X-ray radiation of Cu Kα was used and the measurement range was from 2.0 to 40° (2θ) with a step of 0.020° (2θ).

Single-Crystal X-ray Diffraction. A single crystal of **Co_2-MOF** was mounted on a cryoloop using a viscous hydrocarbon oil to coat the crystal. X-ray data were collected at 120 K on a Supernova diffractometer equipped with a graphite-monochromated Enhance (Mo) X-ray source (λ = 0.71073 Å). (More information in the Supporting Information.)

SEM of Field Emission. FESEM images of **Co_2-MOF** were acquired using an Ultra 55 (Zeiss), operating at 2.0 kV, using powder samples prepared on a sample holder with a double-sided adhesive tape for the dispersion of the sample. Samples were coated with platinum in order to avoid charging effects.

Magnetic Measurements. Magnetic susceptibility measurements were carried out on a polycrystalline sample with a Quantum Design MPMS-XL-5 SQUID susceptometer. The susceptibility data were corrected from the diamagnetic contributions as deduced by using Pascal's constant tables.

X-ray Photoelectron Spectra. X-ray photoelectron spectra of the catalysts were recorded with a SPECS spectrometer equipped with a Phoibos 150 MCD-9 multichannel analyzer using nonmonochromatic Mg Kα (1253.6 eV) irradiation. Spectra were recorded using an analyzer pass energy of 30 eV and an X-ray power of 100 W under an operating pressure of 10−9 mbar. (More information in the Supporting Information.)

Adsorption Measurements. High-resolution adsorption isotherms up to 1 bar were measured in a Micromeritics ASAP 2010. Approximately 150 mg of solid was immersed in a liquid circulation thermostatic bath within a glass sample holder. The samples were degassed overnight at 333 K under high vacuum before each isotherm. Then, CO_2 adsorption isotherms were acquired at 273, 283, 298, 313, and 333 K.

High-pressure adsorption isotherms were evaluated in an IGA-3 gravimetric analyzer (Hiden Isochema). About 50 mg of the sample was loaded into the hanging pan and degassed at 333 K under high vacuum for 4 h. No weight loss was recorded at the end of the degasification process. The sample was then cooled down to the adsorption temperature under vacuum prior to the isotherm acquisition. Pure CO_2 and CH_4 isotherms were measured up to 1 MPa (10 bar) at 283, 298, 313, and 333 K (more information is given in the Supporting Information).

Electrochemical Measurements. Linear scan voltammetric measurements were performed with an AUTOLAB PGSTAT 30, from Eco Chemie B.V, in a three-electrode undivided glass cell, equipped with a gas inlet and thermostated with a water jacket. The counter and reference electrodes were a Pt bar and an Ag|AgCl|NaCl-saturated electrode, respectively. The reference electrode was connected to the cell solution via a salt bridge, and kept at room temperature (25 ± 1 °C) in a nonisothermal configuration. The working electrode was a homemade pyrolytic graphite electrode constructed by fitting a rod of highly oriented pyrolytic graphite from Mineral Technologies into a PEEK (Polyether ether ketone) casing, so that it exposed the edge of the graphite planes with a circular geometric area of 0.07 cm^2. Prior to cobalt MOF coating, graphite electrodes were polished with abrasive P2400 sandpaper, then rinsed with Millipore water, and dried. To modify the electrode, suspensions of 5 mg mL^{-1} of **Co_2-MOF**, hydrolyzed **Co-MOF**, **IrO_2**, or **RuO_2** electrocatalyst in a Nafion solution (5 wt % in lower aliphatic alcohols and 15−20% water solution, from Sigma-Aldrich) were prepared by ultrasonication for 15 min. Then, a volume of ∼5 μL of this suspension was drop-cast onto the graphite electrode and dried at room temperature overnight.

Before electrochemical measurements, the electrode was cycled in the potential range of 0.2−1.3 V at a sweep rate of 50 mV s^{-1} to obtain a stable CV profile. Ohmic drop was compensated using the positive feedback compensation implemented in the instrument. The current density was referred to the geometrical electrode area. (More information in the Supporting Information.)

■ ASSOCIATED CONTENT

Supporting Information

The Supporting Information is available free of charge at https://pubs.acs.org/doi/10.1021/acsami.9b13655.

Experimental procedures employed during this study, chemical analysis of **Co_2-MOF**, PXRD, TG, FESEM, EDX, and XPS results, magnetic, adsorption, and electrochemical measurements (PDF)

Crystallographic data for **Co_2-MOF** (CIF)

■ AUTHOR INFORMATION

Corresponding Author

*E-mail: pasoabur@itq.upv.es. Phone: +34 963 877 819.

ORCID

José Luis Olloqui-Sariego: 0000-0002-3737-9814

Guillermo Mínguez Espallargas: 0000-0001-7855-1003

José L. Jordá: 0000-0002-0304-5680

Fernando Rey: 0000-0003-3227-5669

Pascual Oña-Burgos: 0000-0002-2341-7867

Author Contributions

The paper was written through contributions of all the authors. All the authors have given approval to the final version of the paper.

Notes

The authors declare no competing financial interest.

■ ACKNOWLEDGMENTS

The authors thank Prof. Avelino Corma for discussion and support, and J. Mazarío for XPS analysis and discussion. Program Severo Ochoa SEV-2016-0683 is gratefully acknowledged. S.G.-T. thanks MINECO for a FPU Ph.D. fellowship FPU16/02117. P.O.-B. thanks MEC for his Ramón y Cajal contract RYC-2014-16620. The authors thank the financial support by the Spanish Government (RTI2018-096399-A-I00, RTI2018-101784-B-I00, and CTQ2014-52641-P). In addition, P.O.-B. thanks UPV for his grant PAID-06-18/SP20180172. The Electron Microscopy Service of the UPV is acknowledged for their help in sample characterization.

■ REFERENCES

(1) Jiao, Y.; Zheng, Y.; Jaroniec, M.; Qiao, S. Z. Design of Electrocatalysts for Oxygen- and Hydrogen-Involving Energy Conversion Reactions. *Chem. Soc. Rev.* **2015**, *44*, 2060−2086.

(2) Xia, B. Y.; Yan, Y.; Li, N.; Wu, H. B.; Lou, X. W.; Wang, X. C. A Metal−Organic Framework-Derived Bifunctional Oxygen Electrocatalyst. *Nat. Energy* **2016**, *1*, 15006−15014.

(3) Ma, T. Y.; Dai, S.; Jaroniec, M.; Qiao, S. Z. Metal−Organic Framework Derived Hybrid Co_3O_4-Carbon Porous Nanowire Arrays as Reversible Oxygen Evolution Electrodes. *J. Am. Chem. Soc.* **2014**, *136*, 13925−13931.
(4) Piccinin, S.; Sartorel, A.; Aquilanti, G.; Goldoni, A.; Bonchio, M.; Fabris, S. Water oxidation surface mechanisms replicated by a totally inorganic tetraruthenium-oxo molecular complex. *Proc. Natl. Acad. Sci. U.S.A.* **2013**, *110*, 4917−4922.
(5) Yin, Q.; Tan, J. M.; Besson, C.; Geletii, Y. V.; Musaev, D. G.; Kuznetsov, A. E.; Luo, Z.; Hardcastle, K. I.; Hill, C. L. A Fast Soluble Carbon-Free Molecular Water Oxidation Catalyst Based on Abundant Metals. *Science* **2010**, *328*, 342−345.
(6) Gao, X.; Zhang, H.; Li, Q.; Yu, X.; Hong, Z.; Zhang, X.; Liang, C.; Lin, Z. Hierarchical $NiCo_2O_4$ Hollow Microcuboids as Bifunctional Electrocatalysts for Overall Water-Splitting. *Angew. Chem.* **2016**, *128*, 6398−6402.
(7) Jin, Y.; Wang, H.; Li, J.; Yue, X.; Han, Y.; Shen, P. K.; Cui, Y. Porous MoO_2 Nanosheets as Non-noble Bifunctional Electrocatalysts for Overall Water Splitting. *Adv. Mater.* **2016**, *28*, 3785−3790.
(8) Chen, D.; Chen, C.; Baiyee, Z. M.; Shao, Z.; Ciucci, F. Nonstoichiometric Oxides as Low-Cost and Highly-Efficient Oxygen Reduction/Evolution Catalysts for Low-Temperature Electrochemical Devices. *Chem. Rev.* **2015**, *115*, 9869−9921.
(9) Li, Y.; Dai, H. Recent advances in zinc−air batteries. *Chem. Soc. Rev.* **2014**, *43*, 5257−5275.
(10) Davenport, T. C.; Ahn, H. S.; Ziegler, M. S.; Tilley, T. D. A Molecular Structural Analog of Proposed Dinuclear Active Sites in Cobalt-Based Water Oxidation Catalysts. *Chem. Commun.* **2014**, *50*, 6326−6329.
(11) Passard, G.; Ullman, A. M.; Brodsky, C. N.; Nocera, D. G. Oxygen Reduction Catalysis at a Dicobalt Center: The Relationship of Faradaic Efficiency to Overpotential. *J. Am. Chem. Soc.* **2016**, *138*, 2925−2928.
(12) Kanan, M. W.; Nocera, D. G. In Situ Formation of an Oxygen-Evolving Catalyst in Neutral Water Containing Phosphate and Co^{2+}. *Science* **2008**, *321*, 1072−1075.
(13) Ling, T.; Yan, D. Y.; Jiao, Y.; Wang, H.; Zheng, Y.; Zheng, X.; Mao, J.; Du, X. W.; Hu, Z.; Jaroniec, M.; Qiao, S. Z. Engineering Surface Atomic Structure of Single-Crystal Cobalt (II) Oxide Nanorods for Superior Electrocatalysis. *Nat. Commun.* **2016**, *7*, 12876−12884.
(14) Chen, S.; Qiao, S.-Z. Hierarchically Porous Nitrogen-Doped Graphene $NiCo_2O_4$ Hybrid Paper as an Advanced Electrocatalytic Water-Splitting Material. *ACS Nano* **2013**, *7*, 10190−10196.
(15) Zhu, Y. P.; Ma, T. Y.; Jaroniec, M.; Qiao, S. Z. Self-Templating Synthesis of Hollow Co_3O_4 Microtube Arrays for Highly Efficient Water Electrolysis. *Angew. Chem., Int. Ed.* **2017**, *56*, 1324−1328.
(16) Meng, C.; Ling, T.; Ma, T.-Y.; Wang, H.; Hu, Z.; Zhou, Y.; Mao, J.; Du, X.-W.; Jaroniec, M.; Qiao, S.-Z. Atomically and Electronically Coupled Pt and CoO Hybrid Nanocatalysts for Enhanced Electrocatalytic Performance. *Adv. Mater.* **2017**, *29*, 1604607−1604613.
(17) Ma, T. Y.; Dai, S.; Jaroniec, M.; Qiao, S. Z. Metal−Organic Framework Derived Hybrid Co_3O_4-Carbon Porous Nanowire Arrays as Reversible Oxygen Evolution Electrodes. *J. Am. Chem. Soc.* **2014**, *136*, 13925−13931.
(18) Deng, S.; Zhong, Y.; Zeng, Y.; Wang, Y.; Wang, X.; Lu, X.; Xia, X.; Tu, J. Hollow TiO_2@Co_9S_8 Core−Branch Arrays as Bifunctional Electrocatalysts for Efficient Oxygen /Hydrogen Production. *Adv. Sci.* **2018**, *5*, 1700772−1700780.
(19) Hu, H.; Guan, B.; Xia, B.; Lou, X. W. Designed Formation of Co_3O_4/$NiCo_2O_4$ Double-Shelled Nanocages with Enhanced Pseudocapacitive and Electrocatalytic Properties. *J. Am. Chem. Soc.* **2015**, *137*, 5590−5595.
(20) Jin, H.; Wang, J.; Su, D.; Wei, Z.; Pang, Z.; Wang, Y. In situ Cobalt−Cobalt Oxide/N-Doped Carbon Hybrids As Superior Bifunctional Electrocatalysts for Hydrogen and Oxygen Evolution. *J. Am. Chem. Soc.* **2015**, *137*, 2688−2694.
(21) Zhang, Y.; Ouyang, B.; Xu, J.; Jia, G.; Chen, S.; Rawat, R. S.; Fan, H. J. Rapid Synthesis of Cobalt Nitride Nanowires: Highly Efficient and Low-Cost Catalysts for Oxygen Evolution. *Angew. Chem., Int. Ed.* **2016**, *55*, 8670−8674.
(22) Cheetham, A. K.; Rao, C. N. R. There's Room in the Middle. *Science* **2007**, *318*, 58−59.
(23) Zhao, S.; Wang, Y.; Dong, J.; He, C.-T.; Yin, H.; An, P.; Zhao, K.; Zhang, X.; Gao, C.; Zhang, L.; Lv, J.; Wang, J.; Zhang, J.; Khattak, A. M.; Khan, N. A.; Wei, Z.; Zhang, J.; Liu, S.; Zhao, H.; Tang, Z. Ultrathin Metal−Organic Framework Nanosheets for Electrocatalytic Oxygen Evolution. *Nat. Energy* **2016**, *1*, 16184−16194.
(24) Lu, X.-F.; Liao, P.-Q.; Wang, J.-W.; Wu, J.-X.; Chen, X.-W.; He, C.-T.; Zhang, J.-P.; Li, G.-R.; Chen, X.-M. An Alkaline-Stable, Metal Hydroxide Mimicking Metal−Organic Framework for Efficient Electrocatalytic Oxygen Evolution. *J. Am. Chem. Soc.* **2016**, *138*, 8336−8339.
(25) Manna, P.; Debgupta, J.; Bose, S.; Das, S. K. A Mononuclear Co(II) Coordination Complex Locked in a Confined Space and Acting as an Electrochemical Water-Oxidation Catalyst: A "Ship-in-a-Bottle" Approach. *Angew. Chem., Int. Ed.* **2016**, *55*, 2425−2430.
(26) Wang, S.; Hou, Y.; Lin, S.; Wang, X. Water Oxidation Electrocatalysis by a Zeolitic Imidazolate Framework. *Nanoscale* **2014**, *6*, 9930−9934.
(27) Zhou, W.; Wu, H.; Yildirim, T. Enhanced H_2 Adsorption in Isostructural Metal−Organic Frameworks with Open Metal Sites: Strong Dependence of the Binding Strength on Metal Ions. *J. Am. Chem. Soc.* **2008**, *130*, 15268−15269.
(28) Brown, J. W.; Henderson, B. L.; Kiesz, M. D.; Whalley, A. C.; Morris, W.; Grunder, S.; Deng, H.; Furukawa, H.; Zink, J. I.; Stoddart, J. F.; Yaghi, O. M. Photophysical pore control in an azobenzene-containing metal−organic framework. *Chem. Sci.* **2013**, *4*, 2858−2864.
(29) Mason, J. A.; Veenstra, M.; Long, J. R. Evaluating metal−organic frameworks for natural gas storage. *Chem. Sci.* **2014**, *5*, 32−51.
(30) Llabresixamena, F.; Casanova, O.; Galiassotailleur, R.; Garcia, H.; Corma, A. Metal Organic Frameworks (MOFs) as Catalysts: A Combination of Cu^{2+} and Co^{2+} MOFs as an Efficient Catalyst for Tetralin Oxidation. *J. Catal.* **2008**, *255*, 220−227.
(31) Dhakshinamoorthy, A.; Alvaro, M.; Garcia, H. Commercial metal−organic frameworks as heterogeneous catalysts. *Chem. Commun.* **2012**, *48*, 11275−11288.
(32) Stavila, V.; Talin, A. A.; Allendorf, M. D. MOF-Based Electronic and Opto-Electronic Devices. *Chem. Soc. Rev.* **2014**, *43*, 5994−6010.
(33) Jin, S.; Son, H.-J.; Farha, O. K.; Wiederrecht, G. P.; Hupp, J. T. Energy Transfer from Quantum Dots to Metal−Organic Frameworks for Enhanced Light Harvesting. *J. Am. Chem. Soc.* **2013**, *135*, 955−958.
(34) Hendon, C. H.; Tiana, D.; Walsh, A. Conductive metal−organic frameworks and networks: fact or fantasy? *Phys. Chem. Chem. Phys.* **2012**, *14*, 13120−13132.
(35) Hendon, C. H.; Tiana, D.; Vaid, T. P.; Walsh, A. Thermodynamic and electronic properties of tunable II−VI and IV−VI semiconductor based metal-organic frameworks from computational chemistry. *J. Mater. Chem. C* **2013**, *1*, 95−100.
(36) Tiana, D.; Hendon, C. H.; Walsh, A.; Vaid, T. P. Computational Screening of Structural and Compositional Factors for Electrically Conductive Coordination Polymers. *Phys. Chem. Chem. Phys.* **2014**, *16*, 14463−14472.
(37) Inukai, M.; Horike, S.; Itakura, T.; Shinozaki, R.; Ogiwara, N.; Umeyama, D.; Nagarkar, S.; Nishiyama, Y.; Malon, M.; Hayashi, A.; Ohhara, T.; Kiyanagi, R.; Kitagawa, S. Encapsulating Mobile Proton Carriers into Structural Defects in Coordination Polymer Crystals: High Anhydrous Proton Conduction and Fuel Cell Application. *J. Am. Chem. Soc.* **2016**, *138*, 8505−8511.
(38) Sheberla, D.; Bachman, J. C.; Elias, J. S.; Sun, C.-J.; Shao-Horn, Y.; Dincă, M. Conductive MOF Electrodes for Stable Supercapacitors with High Areal Capacitance. *Nat. Mater.* **2017**, *16*, 220−224.
(39) Miner, E. M.; Fukushima, T.; Sheberla, D.; Sun, L.; Surendranath, Y.; Dinca, M. Electrochemical Oxygen Reduction

Catalysed by Ni_3(hexaiminotriphenylene)$_2$. *Nat. Commun.* **2016**, *7*, 10942−10949.
(40) Shen, J.-Q.; Liao, P.-Q.; Zhou, D.-D.; He, C.-T.; Wu, J.-X.; Zhang, W.-X.; Zhang, J.-P.; Chen, X.-M. Modular and Stepwise Synthesis of a Hybrid Metal−Organic Framework for Efficient Electrocatalytic Oxygen Evolution. *J. Am. Chem. Soc.* **2017**, *139*, 1778−1781.
(41) Tan, K.; Nijem, N.; Canepa, P.; Gong, Q.; Li, J.; Thonhauser, T.; Chabal, Y. J. Stability and Hydrolyzation of Metal Organic Frameworks with Paddle-Wheel SBUs upon Hydration. *Chem. Mater.* **2012**, *24*, 3153−3167.
(42) Hendon, C. H.; Walsh, A. Chemical principles underpinning the performance of the metal−organic framework HKUST-1. *Chem. Sci.* **2015**, *6*, 3674−3683.
(43) Zhang, Z.; Zhang, L.; Wojtas, L.; Eddaoudi, M.; Zaworotko, M. J. Template-Directed Synthesis of Nets Based upon Octahemioctahedral Cages That Encapsulate Catalytically Active Metalloporphyrins. *J. Am. Chem. Soc.* **2012**, *134*, 928−933.
(44) Nguyen, A. I.; Ziegler, M. S.; Oña-Burgos, P.; Sturzbecher-Hohne, M.; Kim, W.; Bellone, D. E.; Tilley, T. D. Mechanistic Investigations of Water Oxidation by a Molecular Cobalt Oxide Analogue: Evidence for a Highly Oxidized Intermediate and Exclusive Terminal Oxo Participation. *J. Am. Chem. Soc.* **2015**, *137*, 12865−12872.
(45) Davies, J. E.; Rivera, A. V.; Sheldrick, M. Tetra-μ-benzoato-bis(4-methylquinoline)dicobalt(II). *Acta Crystallogr., Sect. B: Struct. Crystallogr. Cryst. Chem.* **1977**, *33*, 156−158.
(46) Catterick, J.; Hursthouse, M. B.; Thornton, P.; Welch, A. J. Crystal and molecular structure of tetra-μ-benzoato-bisquinolinedicobalt(II), a binuclear cobalt(II) carboxylate. *J. Chem. Soc., Dalton Trans.* **1977**, 223−226.
(47) Cui, Y.; Zheng, F.; Huang, J. Tetrakis(μ-phenylacetato-O:O′)bis[(quinoline-N)cobalt(II)]. *Acta Crystallogr., Sect. C: Cryst. Struct. Commun.* **1999**, *55*, 1067−1069.
(48) Cui, Y.; Long, D.; Huang, X.; Zheng, F.; Chen, W.; Huang, J. Synthesis and Crystal Structure of a Binuclear Cobalt(II)Carboxylate Complex $Co_2(O_2CCMe_3)_4(C_9H_7N)_2$. *Chin. J. Struct. Chem.* **1999**, *18*, 9−13.
(49) Golubnichaya, M. A.; Sidorov, A. A.; Fomina, I. G.; Eremenko, L. T.; Nefedov, S. E.; Eremenko, I. L.; Moiseev, I. I. Cobalt (II) Binuclear Trimethylacetate Complexes: Synthesis and Structure of $Co_2Py_4(\mu\text{-}OH_2)(\mu\text{-}OOCCMe_3)_2(OOCCMe_3)_2$ and $Co_2Py_2(\mu\text{-}OOCCMe_3)_4$. *Russ. J. Inorg. Chem.* **1999**, *44*, 1401−1410.
(50) Benbellat, N.; Gavrilenko, K. S.; Le Gal, Y.; Cador, O.; Golhen, S.; Gouasmia, A.; Fabre, J.-M.; Ouahab, L. Co(II)−Co(II) Paddlewheel Complex with a Redox-Active Ligand Derived from TTF. *Inorg. Chem.* **2006**, *45*, 10440−10442.
(51) Palomino, M.; Corma, A.; Rey, F.; Valencia, S. New Insights on CO_2−Methane Separation Using LTA Zeolites with Different Si/Al Ratios and a First Comparison with MOFs. *Langmuir* **2010**, *26*, 1910−1917.
(52) Palomino, M.; Corma, A.; Jordá, J. L.; Rey, F.; Valencia, S. Zeolite Rho: a Highly Selective Adsorbent for CO_2/CH_4 Separation Induced by a Structural Phase Modification. *Chem. Commun.* **2012**, *48*, 215−217.
(53) Yaghi, O. M.; Li, H.; Groy, T. L. Construction of Porous Solids from Hydrogen-Bonded Metal Complexes of 1,3,5-benzenetricarboxylic Acid. *J. Am. Chem. Soc.* **1996**, *118*, 9096−9101.
(54) Kim, H. J.; Talukdar, K.; Choi, S.-J. Tuning of Nafion by HKUST-1 as Coordination Network to Enhance Proton Conductivity for Fuel Cell Applications. *J. Nanopart. Res.* **2016**, *18*, 47−53.
(55) Lutful Kabir, M. D.; Kim, H. J.; Choi, S.-J. Highly Proton Conductive Zn(II)-Based Metal−Organic Framework/Nafion Composite Membrane for Fuel Cell Application. *Sci. Adv. Mater.* **2018**, *10*, 1630−1635.
(56) Surendranath, Y.; Kanan, M. W.; Nocera, D. G. Mechanistic Studies of the Oxygen Evolution Reaction by a Cobalt-Phosphate Catalyst at Neutral pH. *J. Am. Chem. Soc.* **2010**, *132*, 16501−16509.
(57) Ullman, A. M.; Brodsky, C. N.; Li, N.; Zheng, S.-L.; Nocera, D. G. Probing Edge Site Reactivity of Oxidic Cobalt Water Oxidation Catalysts. *J. Am. Chem. Soc.* **2016**, *138*, 4229−4236.
(58) Laviron, E.; Roullier, L.; Degrand, C. A multilayer model for the study of space distributed redox modified electrodes. *J. Electroanal. Chem.* **1980**, *112*, 11−23.
(59) Tagliazucchi, M.; Calvo, E. J. Charge Transport in Redox Polyelectrolyte Multilayer Films: The Dramatic Effects of Outmost Layer and Solution Ionic Strength. *ChemPhysChem* **2010**, *11*, 2957−2968.
(60) Liao, P.-Q.; Shen, J.-Q.; Zhang, J.-P. Metal−organic frameworks for electrocatalysis. *Coord. Chem. Rev.* **2018**, *373*, 22−48.